doi:10.1038/nature11211

Supplementary Table 1 | X-ray statistics of data collection and refinement.

	Native	Se-SAD
Data collection		
Space group	$P3_2$	$P3_2$
Cell dimensions		
a, *b*, *c* (Å)	171.55, 171.55, 83.18	168.92, 168.92, 84.25
α, β, γ (º)	90, 90, 120	90, 90, 120
Wavelength (Å)	0.97949	0.97916
Resolution (Å)	50.0–3.2 (3.31–3.20)	50.0–4.15 (4.30–4.15)
Measured reflections	262,889	189,051
Unique reflections	45,536	40,658
R_{merge}	0.186 (0.736)	0.162 (0.469)
$I/\sigma I$	12.8 (3.0)	10.3 (3.6)
Completeness (%)	100 (99.7)	99.7 (99.8)
Redundancy	5.8 (5.6)	4.6 (4.7)
Refinement		
Resolution (Å)	38.12–3.19	
Number of reflections	45,435	
R_{work}/R_{free}	16.83/21.62	
Number of atoms		
Protein	14,034	
RNA	358	
Water	34	
B factors (Å^2)		
Protein	52.47	
RNA	42.6	
Water	28.6	
R.m.s. deviations		
Bond lengths (Å)	0.010	
Bond angles (º)	1.347	

Highest resolution shells are shown in parentheses.

Supplementary Table 2 | Analysis of small-RNA libraries.

Filtering reads	Soluble		Crystalline	
Total reads	27,117,105		26,599,870	
No adaptor sequence	2,489,636	(9.2)	2,246,179	(8.4)
Standard used in library construction	1,230	(0.0)	2,322	(0.0)
Small-RNA reads	24,626,239	(90.8)	24,351,369	(91.5)
Failed quality filter	3,875,605	(15.7)	3,890,220	(16.0)
Passed quality filter	20,750,634	(84.3)	20,461,149	(84.0)
15–24 nt for mapping	1,035,603	(5.0)	1,676,927	(8.2)
8–24 nt with ≥10 reads for scatterplot	10,659,771	(51.4)	11,428,129	(55.9)
Unique sequences for scatterplot	63,144		72,024	

Percentages in parentheses are relative to the parent category. The scatterplot is Supplementary Fig. 5c.

Mapping reads	Soluble				Crystalline			
	Reads		Sequences		Reads		Sequences	
pRSF-KpAGO	846,852	(81.8)	30,884	(23.1)	1,309,717	(78.1)	32,677	(16.9)
Cam^R gene	2,877	(0.3)	684	(0.5)	5,311	(0.3)	891	(0.5)
BL21(DE3)	81,526	(7.9)	39,295	(29.3)	158,596	(9.5)	67,958	(35.2)
Unmapped	104,348	(10.1)	63,086	(47.1)	203,303	(12.1)	91,794	(47.5)
Total	1,035,603	(100)	133,949	(100)	1,676,927	(100)	193,320	(100)

Percentages in parentheses are relative to the total number of 15–24-nucleotide reads or sequences passing the quality filter.

Supplementary Table 3 | Comparison of the crystal structures of KpAGO, TtAGO and NcQDE-2 MID-PIWI lobe. Structures are drawn in ribbon representation, with the N (cyan) and PAZ (magenta) domains highlighted and loops L1 and L2 coloured in blue and green, respectively. Guide strands (red) are shown in stick representation. For clarity, the target strands are not shown in the TtAGO ternary complexes.

Structure	PDB code	Guide 3′ end	Conformation of loop L2	
TtAGO binary complex with a guide DNA	3DLH	PAZ	Unplugged	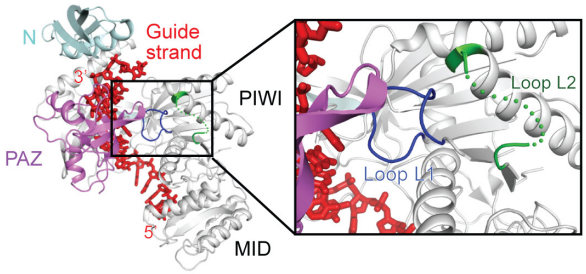
TtAGO ternary complex with guide DNA and target RNA	3F73 3HO1 3HXM	PAZ	Unplugged	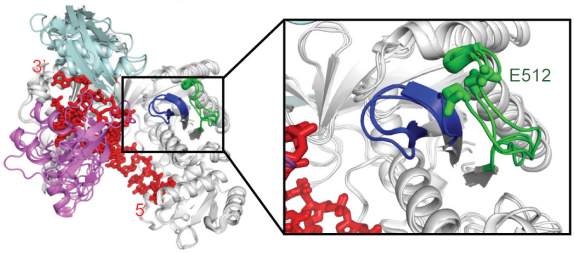
TtAGO ternary complex with guide DNA and target RNA	3HJF 3HK2 3HM9 3HVR	Released	Plugged	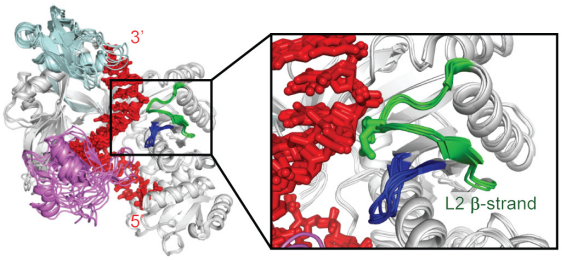
KpAGO binary complex with guide RNA	Current structure	Released	Plugged	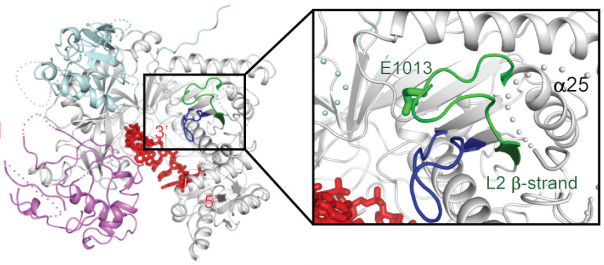
NcQDE-2 MID-PIWI lobe in apo form	2YHA	–	Unplugged	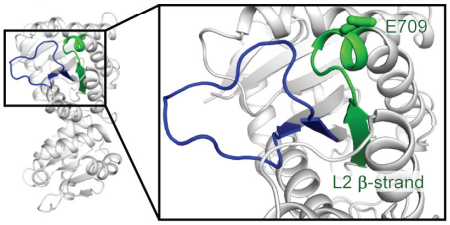

Supplementary Table 4 | Plasmids used and generated in this study.

Plasmid	Description
pRSF-KpAGO	*E. coli* expression plasmid, *K. polysporus AGO1*(207–1251)
pRS402GPD-GFP(S65T)	Integrating plasmid, GFP(S65T) under *GPD* promoter
pRS405TEF-KpDCR1	Integrating plasmid, *K. polysporus DCR1* under *TEF* promoter
pRS404CYC-KpAGO1	Integrating plasmid, *K. polysporus AGO1* under *CYC1* promoter
pRS404CYC-KpAGO1(207–1251)	Integrating plasmid, *K. polysporus AGO1*(207–1251) under *CYC1* promoter
pRS404CYC-FLAG$_3$-KpAGO1	Integrating plasmid, FLAG$_3$-tagged *K. polysporus AGO1* under *CYC1* promoter
pRS404CYC-FLAG$_3$-KpAGO1(Y902L)	Integrating plasmid, FLAG$_3$-tagged *K. polysporus AGO1*(Y902L) under *CYC1* promoter
pRS404CYC-FLAG$_3$-KpAGO1(H977A)	Integrating plasmid, FLAG$_3$-tagged *K. polysporus AGO1*(H977A) under *CYC1* promoter
pRS404CYC-FLAG$_3$-KpAGO1(E1013A)	Integrating plasmid, FLAG$_3$-tagged *K. polysporus AGO1*(E1013A) under *CYC1* promoter
pRS404CYC-FLAG$_3$-KpAGO1(R1045A)	Integrating plasmid, FLAG$_3$-tagged *K. polysporus AGO1*(R1045A) under *CYC1* promoter
pRS404CYC-FLAG$_3$-KpAGO1(D1046A)	Integrating plasmid, FLAG$_3$-tagged *K. polysporus AGO1*(D1046A) under *CYC1* promoter
pRS404CYC-FLAG$_3$-KpAGO1(Q1052A)	Integrating plasmid, FLAG$_3$-tagged *K. polysporus AGO1*(Q1052A) under *CYC1* promoter
pRS404CYC-FLAG$_3$-KpAGO1(E1060A)	Integrating plasmid, FLAG$_3$-tagged *K. polysporus AGO1*(E1060A) under *CYC1* promoter

Supplementary Table 5 | Sequences of RNA oligonucleotides used in this study.

Guide RNA[1]
UAAAGUGCUUAUAGUGCAGGUAG
Passenger RNA
ACCUGCACUAUAAGCACUUUAAG
Guide RNA for 3′ labelling
UAAAGUGCUUAUAGUGCAGGUA
Passenger RNA for 3′ labelling
ACCUGCACUAUAAGCACUUUAA
Perfect-match target for synthetic guide RNA
GGGAGAAACAAAAAUACCUACCUGCACUAUAAGCACUUUACCAUCUCAAACUUACUCAGA
10–11-mismatch target for synthetic guide RNA[2]
GGGAGAAACAAAAAUACCUACCUGCACUA**AU**AGCACUUUACCAUCUCAAACUUACUCAGA
Expected cleavage product for synthetic guide RNA
GGGAGAAACAAAAAUACCUACCUGCACUAU
Perfect-match target for copurifying 17-nucleotide RNA
GGGAGAUAAAUAACCAACUCUUUGAACCAAUAUAUGAAGC
10–11-mismatch target for copurifying 17-nucleotide RNA[2]
GGGAGAUAAAUAACCAACU**GA**UUGAACCAAUAUAUGAAGC
Expected cleavage product for copurifying 17-nucleotide RNA
GGGAGAUAAAUAACCAACUC

[1] 2′-deoxy–substituted guide RNAs used in passenger-strand cleavage studies are depicted in Fig. 3e.
[2] Bases that form mismatches with the guide RNA are bold and underlined.

Supplementary Table 6 | Yeast strains used and generated in this study.

Strain	Genotype	Species	Reference
DPB005	*MATα hoΔ ura3-1*	*S. castellii*	*A*
DPB007	*MATα hoΔ ura3-1 ago1*Δ::Hyg	*S. castellii*	*A*
DPB267	*MATα hoΔ ura3-1 xrn1*Δ::KanMX6	*S. castellii*	This study
DPB268	*MATα hoΔ ura3-1 ago1*Δ::Hyg *xrn1*Δ::KanMX6	*S. castellii*	This study
L4718	*MATα leu2-3,112 trp1-1 can1-100 ura3-1 ade2-1 his3-11,15*	*S. cerevisiae*	*B*
DPB900	*MATα leu2-3,112 trp1-1 can1-100 ura3-1 ADE2::pGPD(empty) his3-11,15*	*S. cerevisiae*	This study
DPB249	*MATα leu2-3,112 trp1-1 can1-100 ura3::GFP(S65T)-KanMX6 ade2-1 his3-11,15*	*S. cerevisiae*	*A*
DPB914	*MATα leu2-3,112 trp1-1 can1-100 ura3::GFP(S65T)-KanMX6 ADE2::pGPD-GFP(S65T) his3-11,15*	*S. cerevisiae*	This study
DPB915	*MATα leu2-3,112 trp1-1 can1-100 ura3::GFP(S65T)-KanMX6 ADE2::pGPD-GFP(S65T) HIS3::pGAL1-strongSC_GFP*	*S. cerevisiae*	This study
DPB901	*MATα LEU2::pTEF-KpDCR1 trp1-1 can1-100 ura3::GFP(S65T)-KanMX6 ADE2::pGPD-GFP(S65T) HIS3::pGAL1-strongSC_GFP*	*S. cerevisiae*	This study
DPB916	*MATα LEU2::pTEF-KpDCR1 TRP1::pCYC-KpAGO1 can1-100 ura3::GFP(S65T)-KanMX6 ADE2::pGPD-GFP(S65T) HIS3::pGAL1-strongSC_GFP*	*S. cerevisiae*	This study
DPB917	*MATα LEU2::pTEF-KpDCR1 TRP1::pCYC-KpAGO1(207–1251) can1-100 ura3::GFP(S65T)-KanMX6 ADE2::pGPD-GFP(S65T) HIS3::pGAL1-strongSC_GFP*	*S. cerevisiae*	This study
DPB906	*MATα LEU2::pTEF-KpDCR1 TRP1::pCYC-FLAG$_3$-KpAGO1 can1-100 ura3::GFP(S65T)-KanMX6 ADE2::pGPD-GFP(S65T) HIS3::pGAL1-strongSC_GFP*	*S. cerevisiae*	This study
DPB907	*MATα LEU2::pTEF-KpDCR1 TRP1::pCYC-FLAG$_3$-KpAGO1(Y902L) can1-100 ura3::GFP(S65T)-KanMX6 ADE2::pGPD-GFP(S65T) HIS3::pGAL1-strongSC_GFP*	*S. cerevisiae*	This study
DPB908	*MATα LEU2::pTEF-KpDCR1 TRP1::pCYC-FLAG$_3$-KpAGO1(H977A) can1-100 ura3::GFP(S65T)-KanMX6 ADE2::pGPD-GFP(S65T) HIS3::pGAL1-strongSC_GFP*	*S. cerevisiae*	This study
DPB909	*MATα LEU2::pTEF-KpDCR1 TRP1::pCYC-FLAG$_3$-KpAGO1(E1013A) can1-100 ura3::GFP(S65T)-KanMX6 ADE2::pGPD-GFP(S65T) HIS3::pGAL1-strongSC_GFP*	*S. cerevisiae*	This study
DPB910	*MATα LEU2::pTEF-KpDCR1 TRP1::pCYC-FLAG$_3$-KpAGO1(R1045A) can1-100 ura3::GFP(S65T)-KanMX6 ADE2::pGPD-GFP(S65T) HIS3::pGAL1-strongSC_GFP*	*S. cerevisiae*	This study
DPB911	*MATα LEU2::pTEF-KpDCR1 TRP1::pCYC-FLAG$_3$-KpAGO1(D1046A) can1-100 ura3::GFP(S65T)-KanMX6 ADE2::pGPD-GFP(S65T) HIS3::pGAL1-strongSC_GFP*	*S. cerevisiae*	This study
DPB912	*MATα LEU2::pTEF-KpDCR1 TRP1::pCYC-FLAG$_3$-KpAGO1(Q1052A) can1-100 ura3::GFP(S65T)-KanMX6 ADE2::pGPD-GFP(S65T) HIS3::pGAL1-strongSC_GFP*	*S. cerevisiae*	This study
DPB913	*MATα LEU2::pTEF-KpDCR1 TRP1::pCYC-FLAG$_3$-KpAGO1(E1060A) can1-100 ura3::GFP(S65T)-KanMX6 ADE2::pGPD-GFP(S65T) HIS3::pGAL1-strongSC_GFP*	*S. cerevisiae*	This study

A. Drinnenberg, et al. RNAi in budding yeast. *Science* **326**, 544-50 (2009).
B. Thomas & Rothstein. Elevated recombination rates in transcriptionally active DNA. *Cell* **56**, 619-30 (1989).

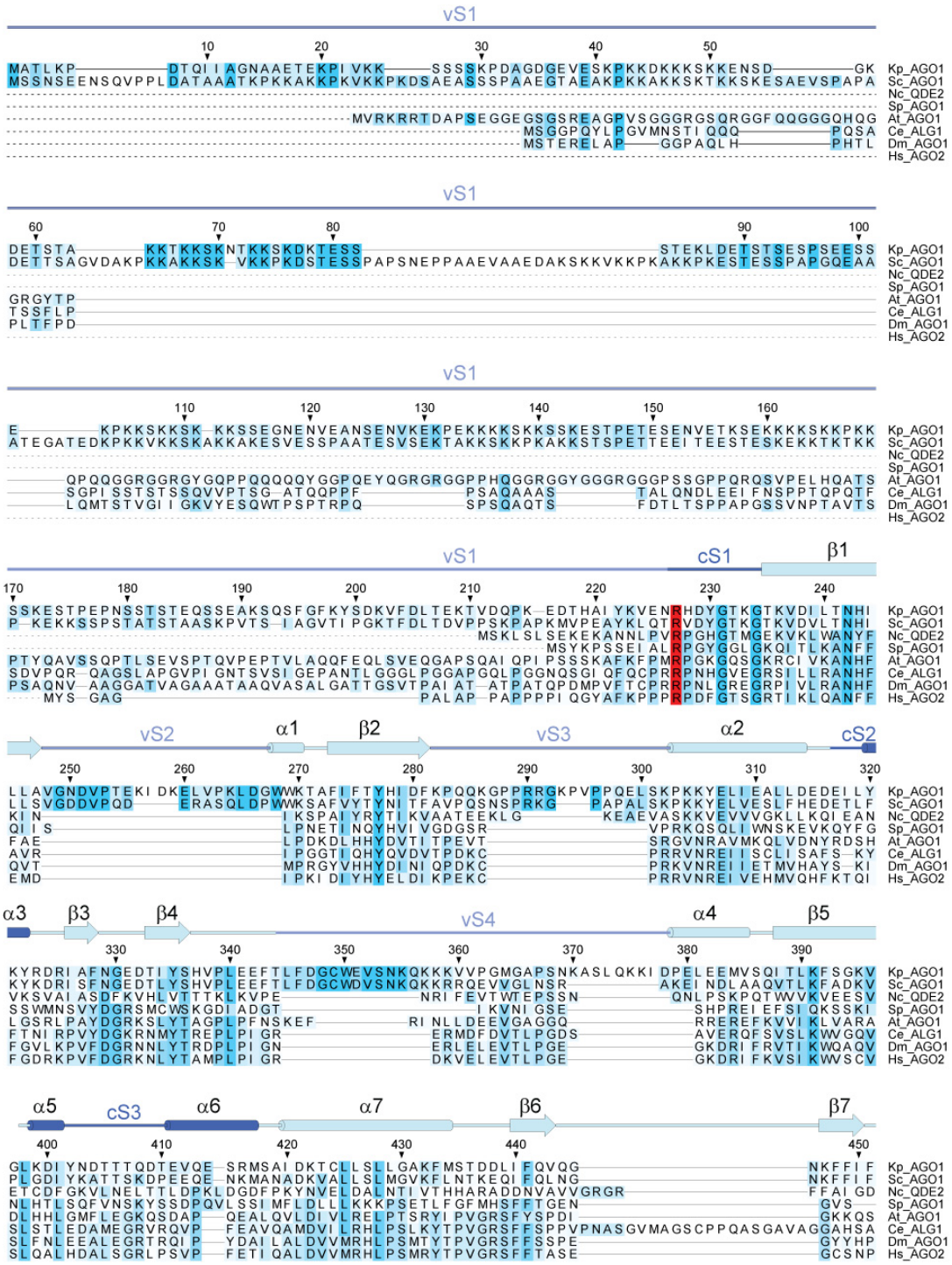
vS1
vS2
vS3
vS4
cS1
cS2
cS3
α1
α2
α3
α4
α5
α6
α7
β1
β2
β3
β4
β5
β6
β7
Kp_AGO1
Sc_AGO1
Nc_QDE2
Sp_AGO1
At_AGO1
Ce_ALG1
Dm_AGO1
Hs_AGO2

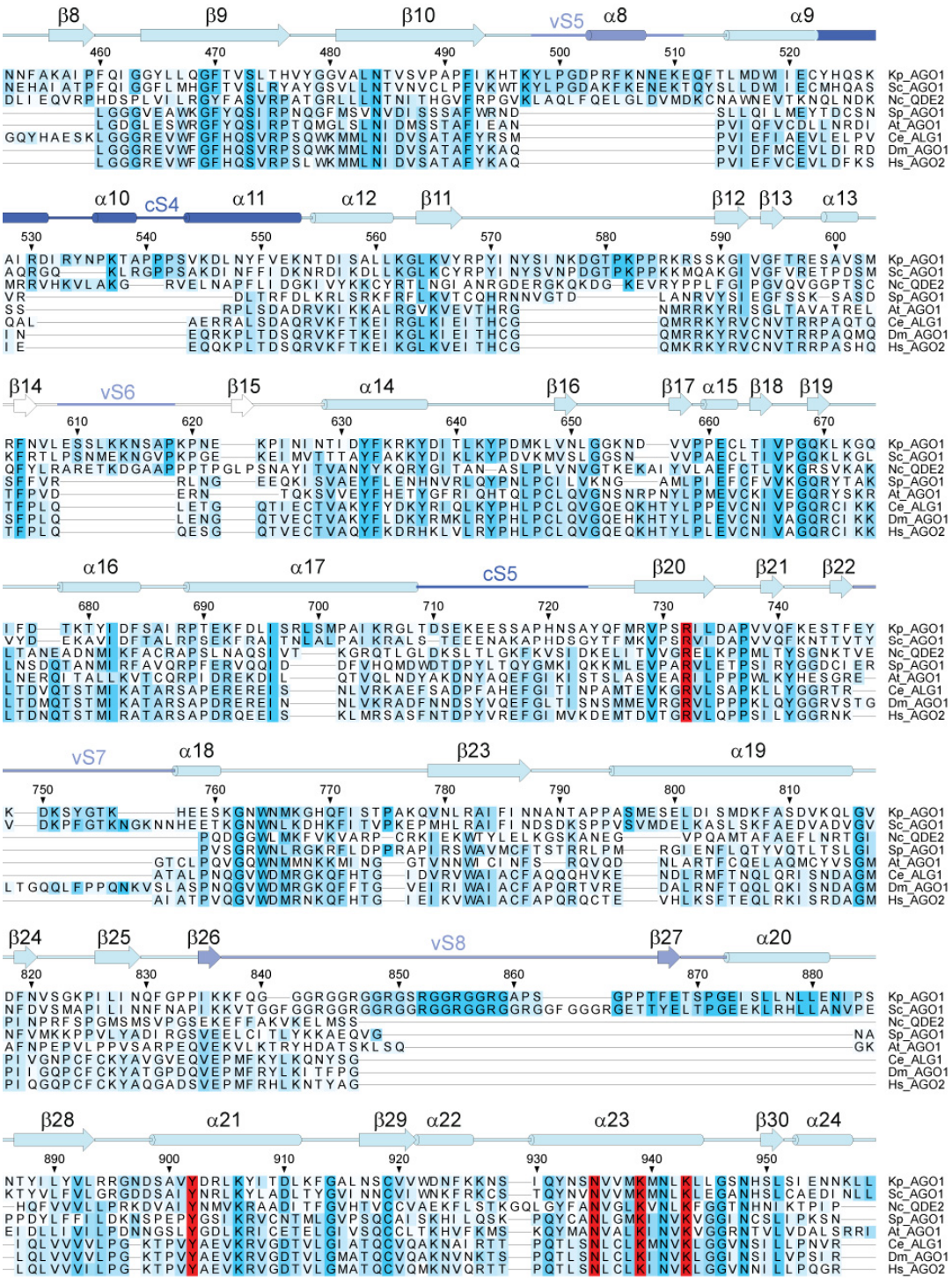
β8 β9 β10 vS5 α8 α9
460 470 480 490 500 510 520
Kp_AGO1
Sc_AGO1
Nc_QDE2
Sp_AGO1
At_AGO1
Ce_ALG1
Dm_AGO1
Hs_AGO2
α10 cS4 α11 α12 β11 β12 β13 α13
530 540 550 560 570 580 590 600
Kp_AGO1
Sc_AGO1
Nc_QDE2
Sp_AGO1
At_AGO1
Ce_ALG1
Dm_AGO1
Hs_AGO2
β14 vS6 β15 α14 β16 β17 α15 β18 β19
610 620 630 640 650 660 670
Kp_AGO1
Sc_AGO1
Nc_QDE2
Sp_AGO1
At_AGO1
Ce_ALG1
Dm_AGO1
Hs_AGO2
α16 α17 cS5 β20 β21 β22
680 690 700 710 720 730 740
Kp_AGO1
Sc_AGO1
Nc_QDE2
Sp_AGO1
At_AGO1
Ce_ALG1
Dm_AGO1
Hs_AGO2
vS7 α18 β23 α19
750 760 770 780 790 800 810
Kp_AGO1
Sc_AGO1
Nc_QDE2
Sp_AGO1
At_AGO1
Ce_ALG1
Dm_AGO1
Hs_AGO2
β24 β25 β26 vS8 β27 α20
820 830 840 850 860 870 880
Kp_AGO1
Sc_AGO1
Nc_QDE2
Sp_AGO1
At_AGO1
Ce_ALG1
Dm_AGO1
Hs_AGO2
β28 α21 β29 α22 α23 β30 α24
890 900 910 920 930 940 950
Kp_AGO1
Sc_AGO1
Nc_QDE2
Sp_AGO1
At_AGO1
Ce_ALG1
Dm_AGO1
Hs_AGO2

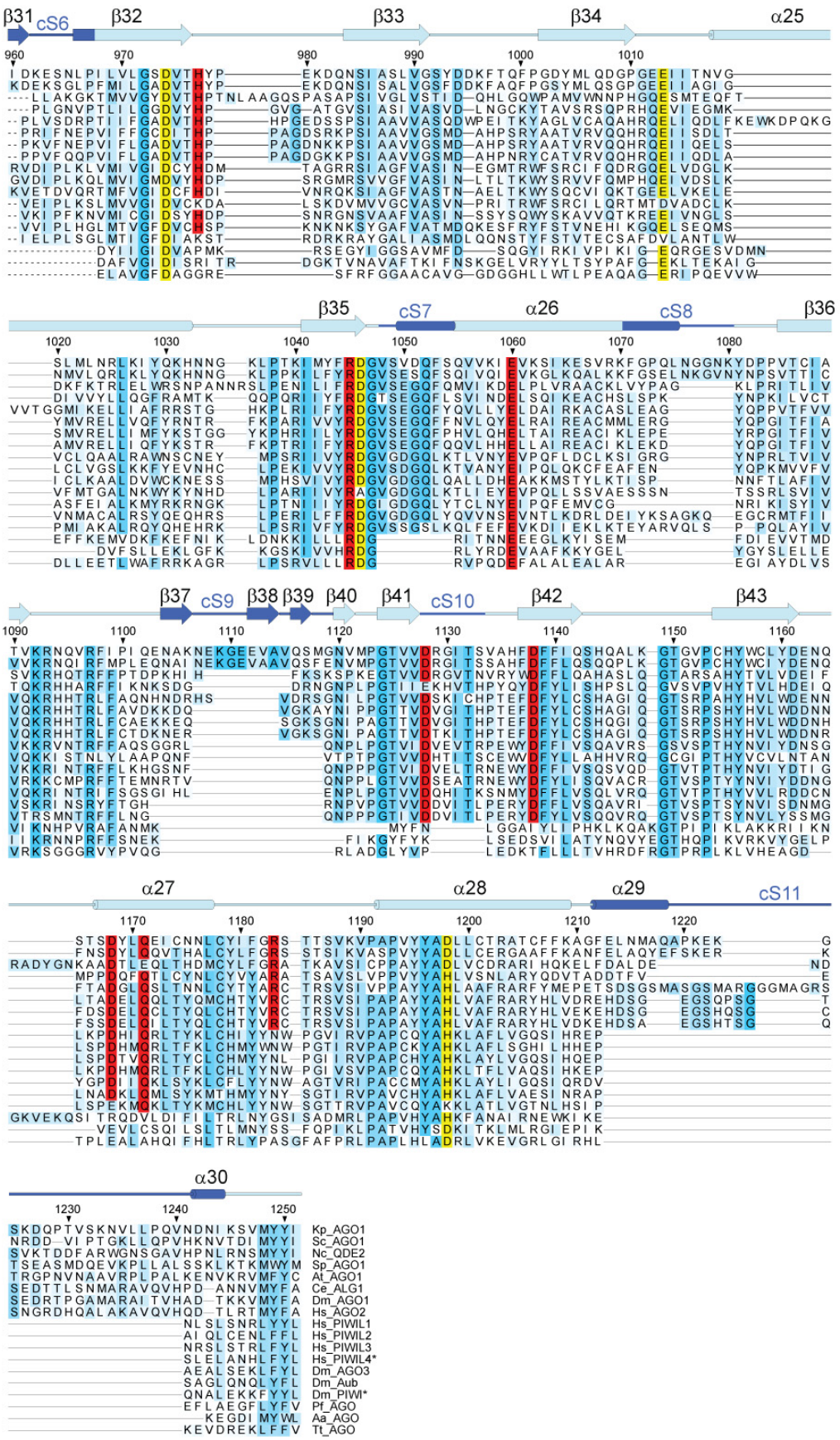
β31 cS6 β32 β33 β34 α25
960 970 980 990 1000 1010
Kp_AGO1
Sc_AGO1
Nc_QDE2
Sp_AGO1
At_AGO1
Ce_ALG1
Dm_AGO1
Hs_AGO2
Hs_PIWIL1
Hs_PIWIL2
Hs_PIWIL3
Hs_PIWIL4*
Dm_AGO3
Dm_Aub
Dm_PIWI*
Pf_AGO
Aa_AGO
Tt_AGO
β35 cS7 α26 cS8 β36
1020 1030 1040 1050 1060 1070 1080
β37 cS9 β38 β39 β40 β41 cS10 β42 β43
1090 1100 1110 1120 1130 1140 1150 1160
α27 α28 α29 cS11
1170 1180 1190 1200 1210 1220
α30
1230 1240 1250

Supplementary Figure 1 | Sequence alignment of the AGO family. Protein sequences were aligned across their length (eukaryotic AGOs) or across their PIWI domain (prokaryotic AGOs and eukaryotic PIWI-clade proteins). Highlighted are the four residues of the catalytic tetrad (yellow), other residues analysed in this work (red), and additional well-conserved amino acids (blue; intensity indicates degree of conservation). Residue numbers and the secondary structure of KpAGO are indicated above the alignment. Kp, *K. polysporus*; Sc, *S. castellii*; Nc, *N. crassa*; Sp, *S. pombe*; At, *A. thaliana*; Ce, *Caenorhabditis elegans*; Dm, *Drosophila melanogaster*; Hs, *H. sapiens*; Pf, *P. furiosus;* Aa, *A. aeolicus*; and Tt, *T. thermophilus*. PIWI-clade proteins for which the residue corresponding to Glu 1013 is not conserved are indicated (*); each of these also contains a non-conserved amino acid at the position of one of the previously proposed active-site residues.

a

	Δ*xrn1*		Δ*xrn1* Δ*ago1*		Δ*xrn1* sampled	
Total tags	2,513,306		1,739,201			
20–21-nt tags	2,467,140	(98.2)	1,709,290	(98.3)		
Tags mapping to genome	1,796,442	(72.8)	1,322,341	(77.4)		
Tags mapping to ORF sense	589,721	(32.8)	293,400	(22.2)		
Tags mapping to ORF antisense	33,605	(1.9)	19,547	(1.5)		
Tags mapping to Y′ consensus	23,142	(1.3)	2,010	(0.2)	11,239	
Tags mapping to Y′ mRNA	17,972	(77.7)	1,559	(77.6)	8,699	(77.4)
Tags mapping to Y′ antisense	5,170	(22.3)	451	(22.4)	2,540	(22.6)

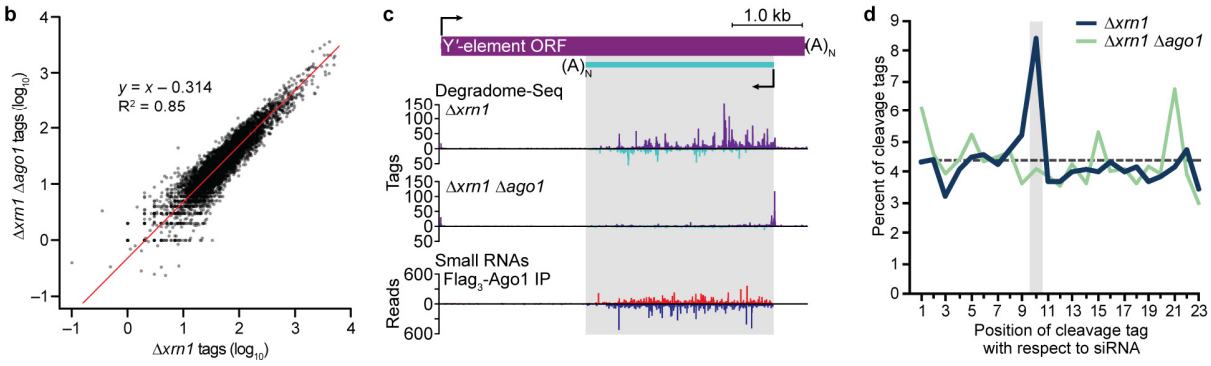

Supplementary Figure 2 | Analysis of *S. castellii* degradome libraries. a, Distribution of degradome tags sequenced from *XRN1*-deletion (Δ*xrn1*) and *XRN1*/*AGO1*-deletion (Δ*xrn1* Δ*ago1*) strains. 20–21-nucleotide sequences were first mapped to the *S. castellii* genome, allowing no mismatches and recovering all hits. The number of genome-mapping reads corresponding to annotated ORFs or the consensus Y′ element are indicated, with percentages shown in parenthesis relative to the parent category. A subset of the complete Δ*xrn1* degradome library was generated to control for library size (Δ*xrn1* sampled; 49% of complete library). **b,** Regression used for library normalization. For each annotated ORF, the number of tags mapping in the sense orientation to annotated exons was calculated by summing the hit-normalized reads. Genes for which either of the strains had zero reads, and ORFs for which there was no annotated homolog in *S. cerevisiae*, were excluded. Red line, result of linear regression performed on log-transformed tag counts between the two strains. **c**, Degradome-cleavage tags mapping to the *S. castellii* Y′ element. The number of tags mapping to the consensus Y′ element are plotted for each position. Above axis, tags from Y′ mRNA; below axis, tags from antisense transcript. For comparison, mapping of Ago1-associated siRNAs, redrawn from Drinnenberg et al. (2009), is shown. **d**, Pairing between cleavage tags and endogenous siRNAs. Degradome tags and siRNAs mapping to the Y′ element were evaluated for antisense overlap between the 5′ ends of the tags and the bodies of the siRNAs. Plotted is the fraction of tags with 5′ ends mapping across from each position within the siRNA. Dashed line, background uniform distribution; gray shading, pairing register expected for AGO cleavage.

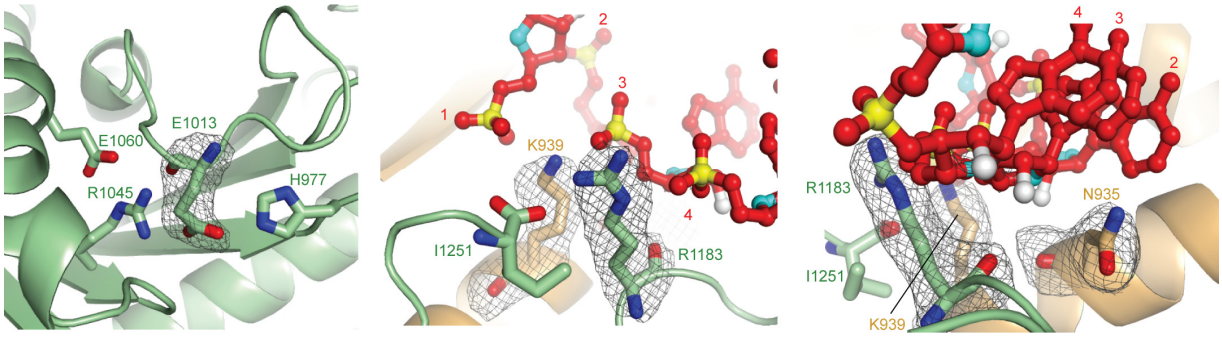

Supplementary Figure 3 | Representative electron density for KpAGO. Simulated-annealing omit map contoured at 4.2σ around Glu 1013 (left); Lys 939 and Arg 1183 (middle); or Asn 935, Lys 939 and Arg 1183 (right). Protein and RNA segments are drawn and coloured as in Fig. 3a.

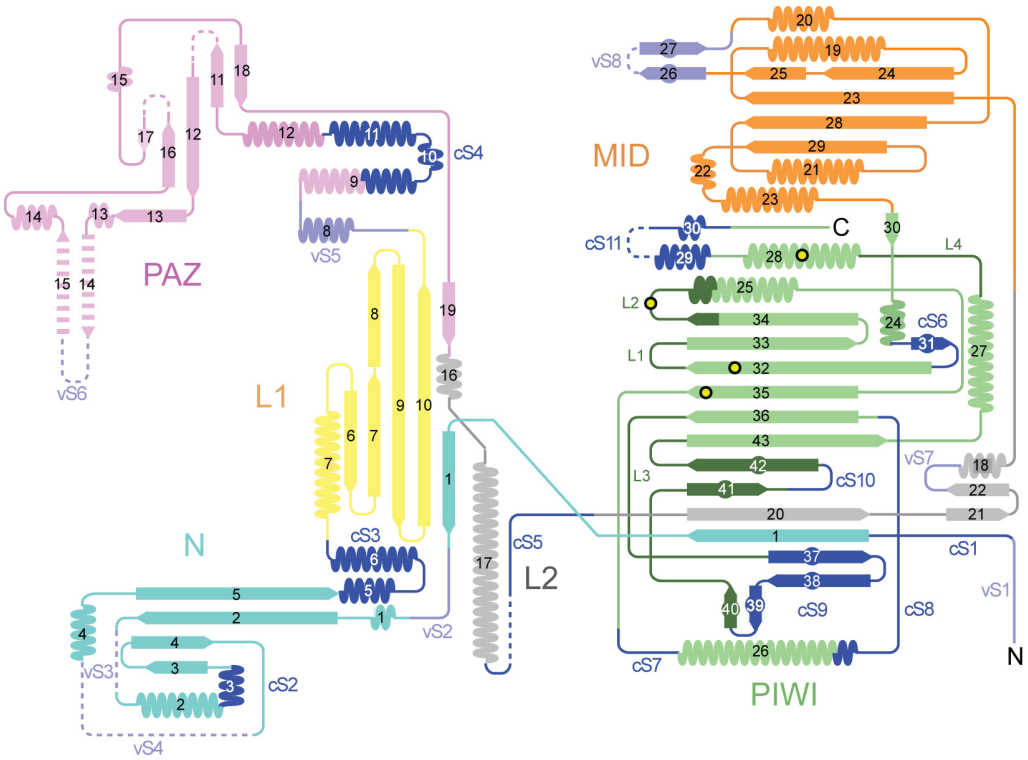

Supplementary Figure 4 | Secondary structure and topology diagram of KpAGO. The domain designations and colours are as in Fig. 2a. The helices and sheets are shown as wavy lines and arrows, respectively. Loops L1, L2, L3 and L4 are highlighted in dark green; active-site residues are indicated as yellow-filled circles.

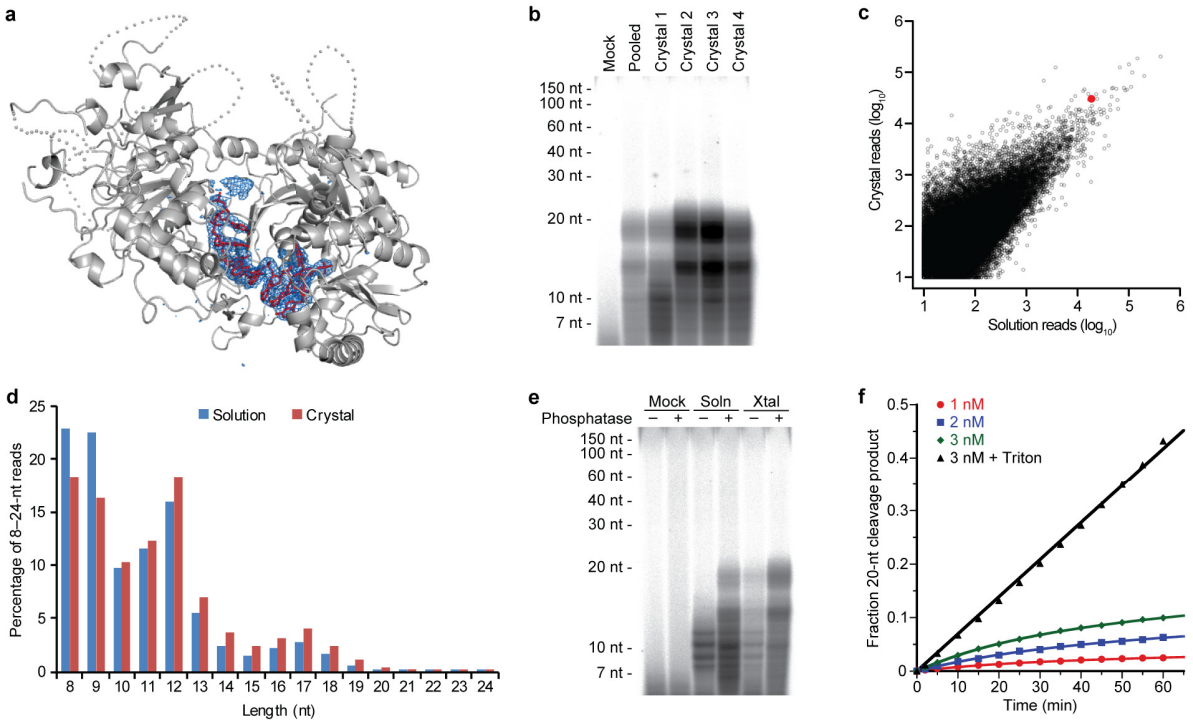

Supplementary Figure 5 | Analyses of copurifying RNAs. a, Simulated-annealing omit map (blue) contoured at 3.5σ around the final RNA model (red). **b**, Copurifying RNA associated with a pool of crystals (pooled) and individual crystals (1–4). Copurifying RNA was extracted and analysed as in Fig. 2d. The variability between individual crystals implies that RNA associated with the rare crystals that diffracted well might differ from that analysed in other crystals, which might explain why 12-nucleotide passenger-strand cleavage fragments (Supplementary Fig. 7) were not observed in the KpAGO structure. **c**, Diverse RNAs copurify with KpAGO (Supplementary Table 2). Shown are the number of reads for a given sequence in small-RNA libraries prepared from soluble (x axis) and crystalline (y axis) KpAGO. Red point, 17-nucleotide copurifying RNA species used in cleavage assays. **d**, Bimodal length distribution of copurifying RNAs. Shown is the percent of reads with the indicated length in small-RNA libraries prepared from soluble and crystalline KpAGO. **e**, Phosphatase-dependence of 5′ end-labelling for most copurifying RNAs. Extracted polynucleotides (or a water-only control, mock) were untreated (–) or treated with phosphatase (+) before 5′ end-labelling with kinase. Otherwise, as in panel **b**. **f**, Kinetics of cleavage guided by a 17-nucleotide copurifying RNA. Reactions containing 1 nM cap-labelled RNA and the indicated concentration of KpAGO were incubated for the indicated time in 1× reaction buffer as in Fig. 2f. Reactions were without Triton, unless otherwise indicated. Plotted are average values of two replicates. Solid lines, least-squares fits to a line (Triton condition) or the burst equation (all others).

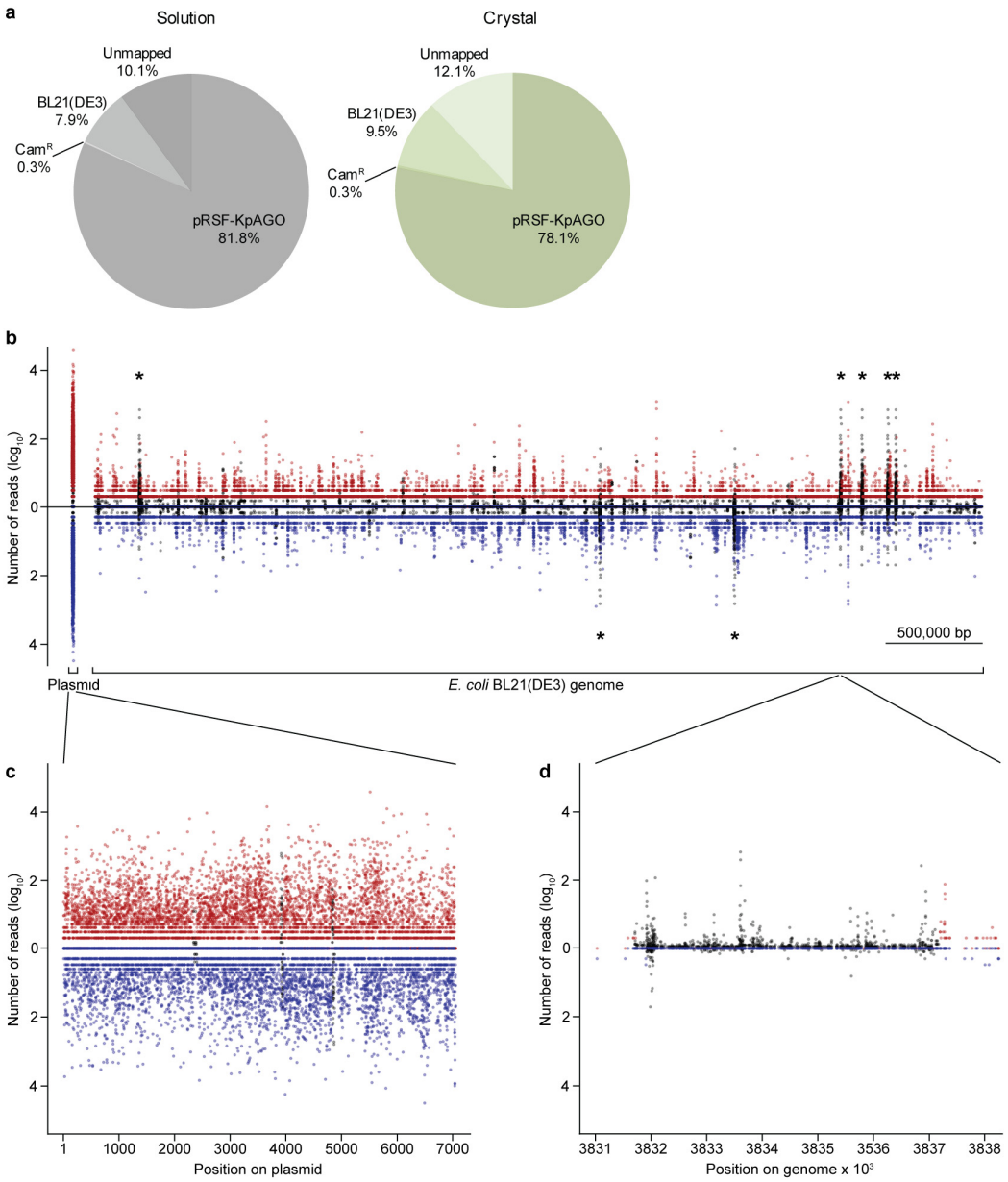

Supplementary Figure 6 | Origins of copurifying RNAs. a, Fraction of reads in small-RNA libraries that map to the KpAGO expression plasmid (pRSF-KpAGO), the chloramphenicol-resistance gene present on pRARE2 in Rosetta2 strains (Cam^R), and the *E. coli* BL21(DE3) genome (Supplementary Table 2). **b**, Loci corresponding to copurifying RNAs. Plotted are the number of small-RNA 5′ ends (solution library) mapping to the indicated position on the KpAGO plasmid (left) or *E. coli* genome (right). Red, uniquely aligned plus-strand reads; blue, uniquely aligned minus-strand reads; black, non-uniquely mapping reads (which were hit-normalized, and thus evenly distributed among their corresponding loci). The seven rRNA loci that are abundant sources of copurifying RNAs are indicated (*). **c**, Close-up view of plasmid-mapping reads, plotted as in panel **b**. The abundance of plasmid-matching copurifying RNAs could be attributed to the high copy number of the plasmid or its propensity to generate double-stranded RNA. **d**, Close-up view of one of seven ribosomal RNA loci, plotted on the same scale as panel c.

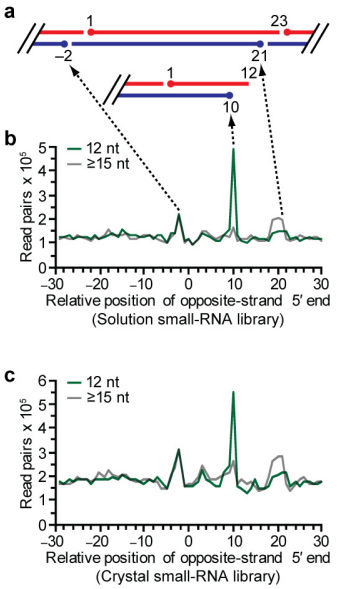

Supplementary Figure 7 | Relationships between copurifying RNAs from opposite strands. **a**, Schematic of relationships expected for 23-nucleotide RNase III cleavage products (top) and those expected for guide RNA–passenger strand cleavage product (bottom). **b**, **c**, Observed relationships between opposite-strand RNAs extracted from soluble (**b**) or crystalline (**c**) KpAGO. Loci of sequences mapping to the plasmid were compared, recording the relative positions of 5′ termini. Plotted in green are the numbers of pairs involving 12-nucleotide RNAs from one strand and ≥15-nucleotide RNAs from the other. Plotted in black are the numbers of pairs involving ≥15-nucleotide RNAs from opposite strands.

The observation that copurifying RNAs matched both strands of the KpAGO expression plasmid, together with the 5′-monophosphate chemistry of the RNA, suggested origins from double-stranded RNAs that were processed by *E. coli* RNase III, which would yield some siRNA-like duplexes with two-nucleotide 3′ overhangs (Xiao et al., 2009). Consistent with this model, the 5′ ends of reads originating from opposite strands tended to be related by a two-nucleotide 3′ overhang (peaks at –2 and +21). Because the 3′ fragment of the cleaved passenger strand is 12 nucleotides (regardless of the initial siRNA duplex length), the enrichment for 12-nucleotide copurifying RNAs (Supplementary Fig. 5d) suggested that they might reflect the 3′ fragments of cleaved passenger strands that remained within KpAGO during purification (and then presumably dissociated during formation of well-diffracting crystals). A striking 10-nucleotide phasing observed between 12-nucleotide RNAs and 15–24-nucleotide opposite-strand pairs strongly supported this biogenesis mechanism (green lines, peak at +10).

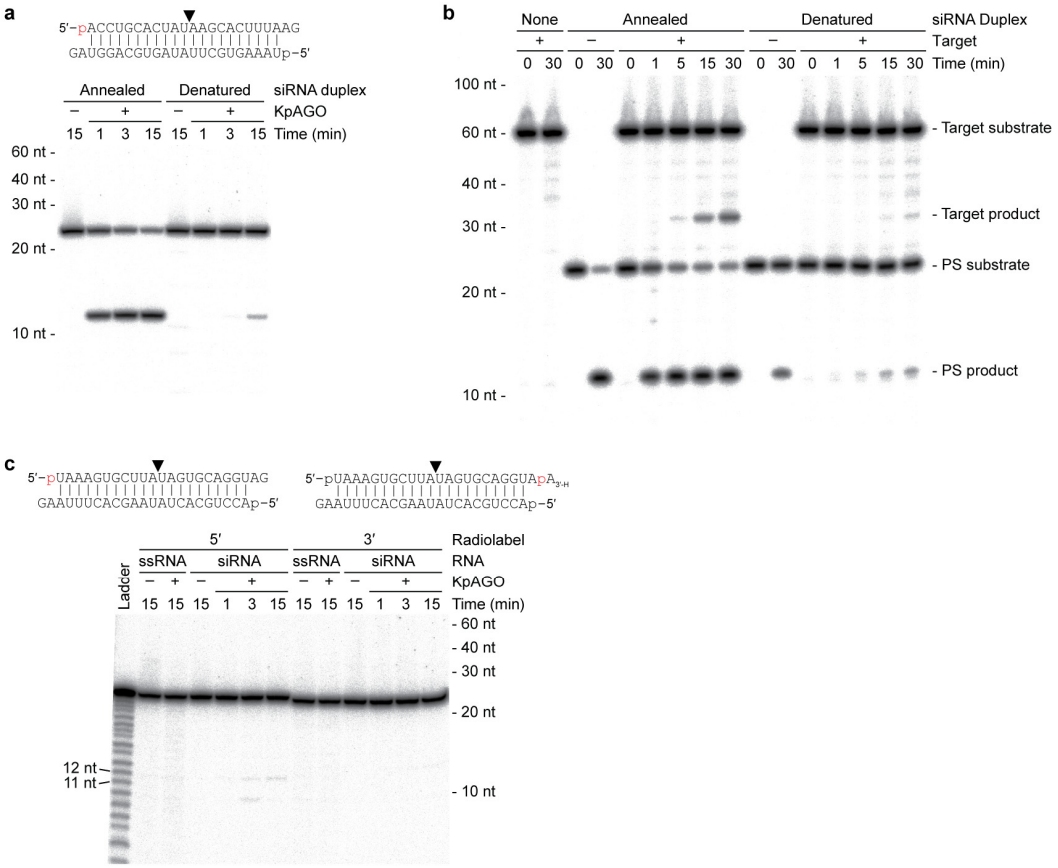

Supplementary Figure 8 | Autonomous activities of recombinant KpAGO. a, Duplex dependence of passenger-strand cleavage. To confirm that the observed cleavage of labelled passenger strands occurred in the context of an siRNA duplex (rather than denatured single-stranded guide RNA that loaded into KpAGO and cleaved a single-stranded passenger RNA), siRNA duplex was denatured at 90 °C for five min and kept on ice before adding KpAGO. The dramatically reduced passenger-strand cleavage activity indicates that the preferred substrate is an siRNA duplex (with residual cleavage of the denatured duplex attributed to re-annealing during the reaction). Passenger-strand cleavage reactions saturated at duplex concentrations far below that of the protein, presumably because most of the protein was already loaded with guide RNA. **b**, Sequential passenger-strand cleavage and target cleavage. Reactions were as in Fig. 2h except without pre-incubation and using end-labelled passenger RNA. The substrates and specific products of passenger-strand (PS) and target cleavage are indicated. The observed kinetics were consistent with rapid passenger-strand cleavage followed by slow release of cleavage fragments to form active RISC, which then cleaves target RNA. **c**, Asymmetric siRNA loading and passenger-strand cleavage by recombinant KpAGO. This experiment was performed together with that shown in Fig. 2g and was the same as Fig. 2g, except the other strand was labelled. The reduced cleavage of the strand beginning with uridine compared to that of the strand beginning with adenosine (Fig. 2g) can be attributed to asymmetric loading of the duplex, with a preference for selecting as the guide the strand beginning with uridine. Denaturing polyacrylamide gel analysis included a lane with partial alkaline-cleavage products (ladder); 11- and 12-nucleotide hydrolysis products are indicated. Note that alkaline-cleavage products (which carry a 2′,3′-cyclic phosphate) migrate approximately one nucleotide faster than do AGO-cleavage products.

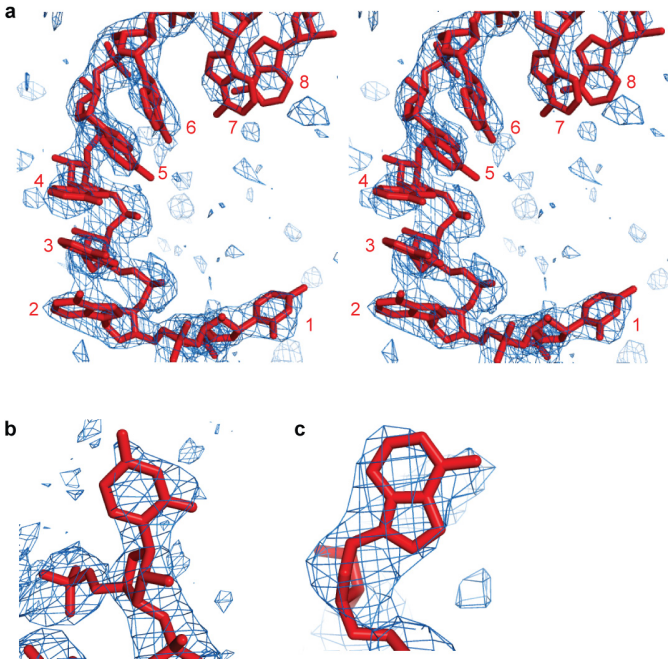

Supplementary Figure 9 | Electron density observed for the guide RNA. a, Stereoview of $F_o - F_c$ electron density map (blue) at 2.6σ around the nucleic-acid-binding channel. The RNA model (red) is drawn as a stick representation with nucleotides numbered from the 5′ end. **b**, **c**, Close-up view of electron density corresponding to the first (**b**) and second (**c**) nucleotides of the guide RNA.

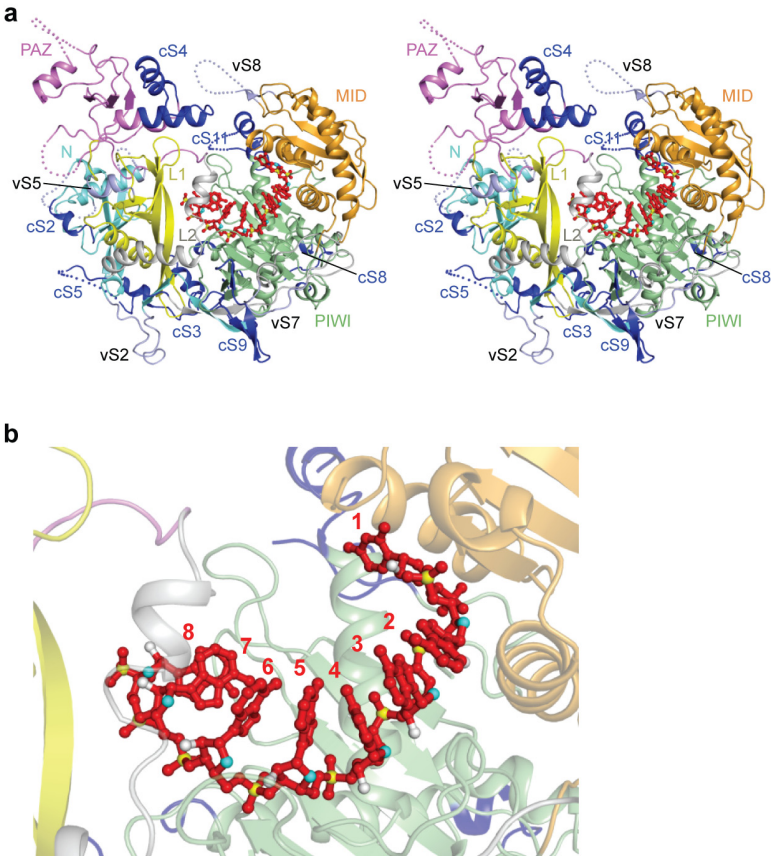

Supplementary Figure 10 | Structure of KpAGO with guide RNA. a, Stereoview of the KpAGO–guide RNA binary complex structure. KpAGO is drawn as in Fig. 2a. Guide RNA (red) is drawn as a stick representation with the 2′-OH groups, O4′ atoms and phosphate atoms coloured in white, cyan and yellow, respectively. **b,** Close-up view of the guide RNA (red). Colours are as in panel **a**, and nucleotides are numbered from the 5′ end.

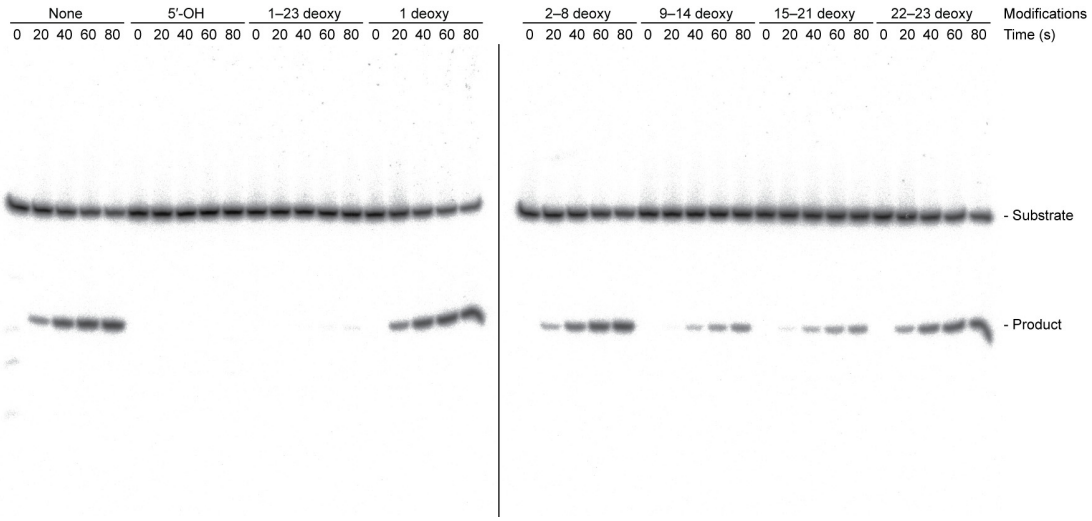

Supplementary Figure 11 | Representative gels of passenger-strand cleavage kinetics. Passenger-strand cleavage assays were performed as described in Fig. 3e. Shown is a phosphorimager scan of a denaturing polyacrylamide gel resolving the substrate and cleavage product.

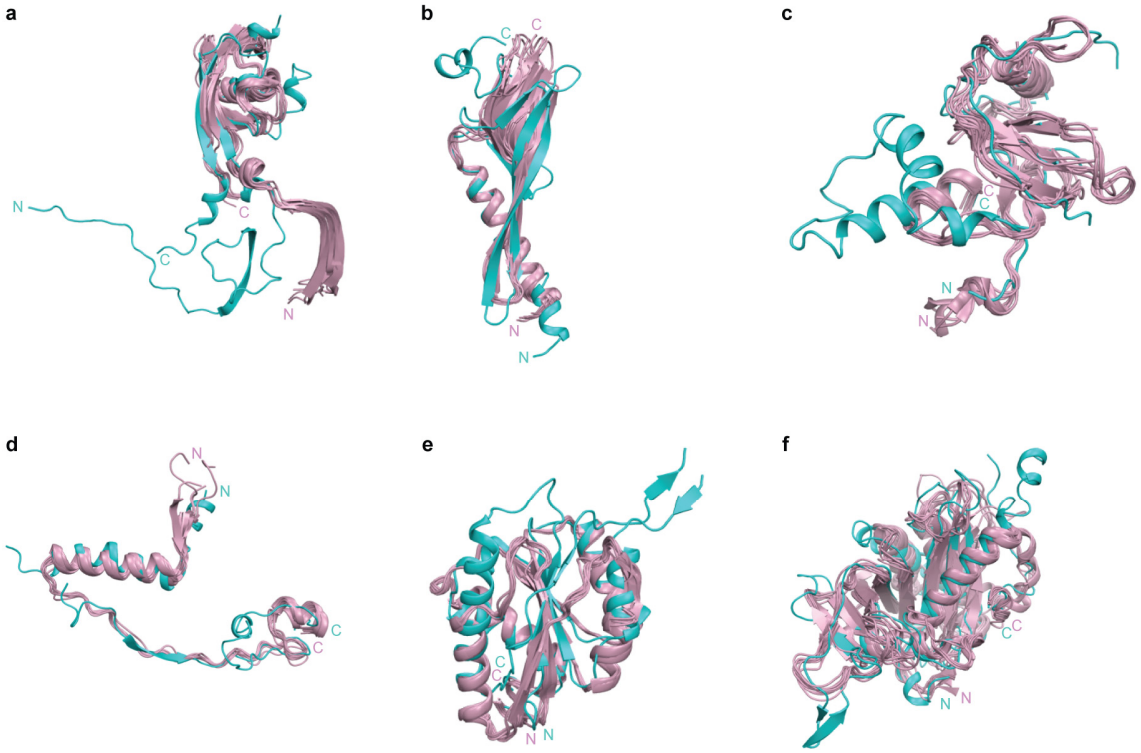

Supplementary Figure 12 | Structural alignment of individual domains. Superpositions of the KpAGO (cyan) and TtAGO structures (pink) on their N (**a**), L1 (**b**), PAZ (**c**), L2 (**d**), MID (**e**) and PIWI (**f**) domains. The PDB codes of TtAGO are 3DLB, 3DLH, 3F73, 3HO1, 3HXM, 3HJF, 3HK2, 3HM9 and 3HVR.

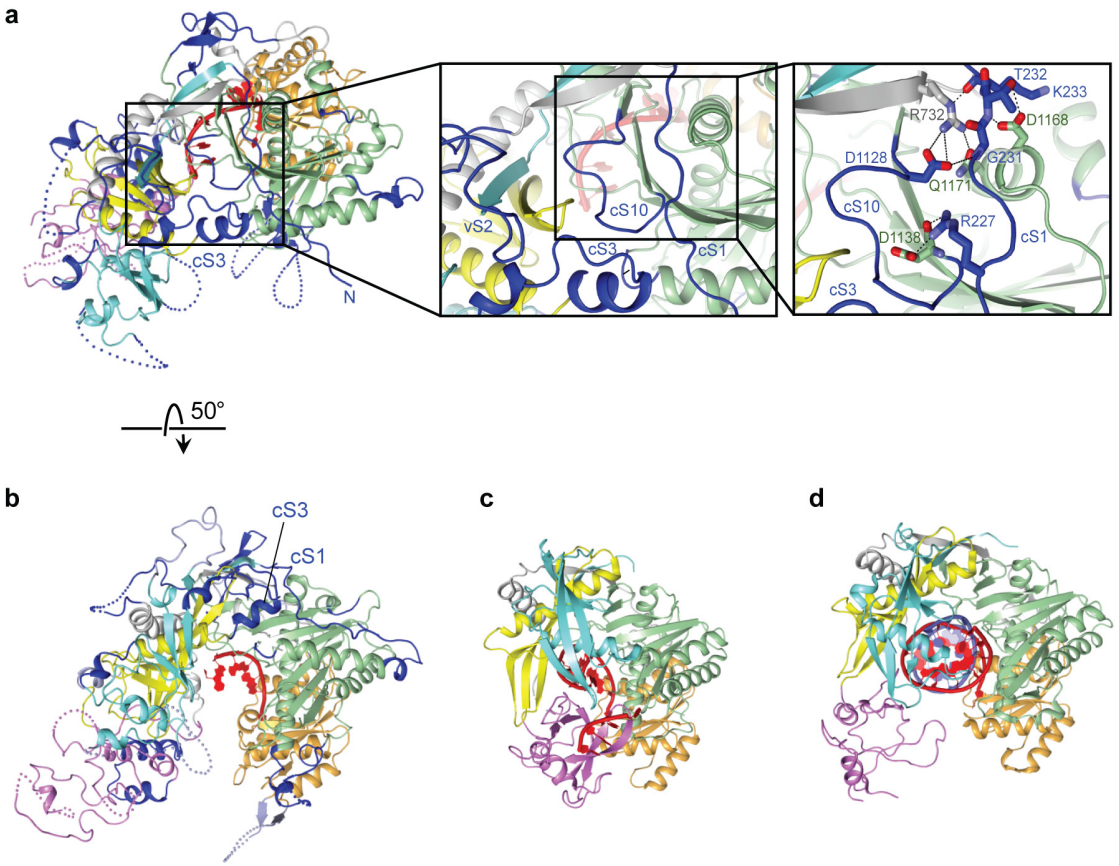

Supplementary Figure 13 | The nucleic-acid-binding channels in eukaryotic and prokaryotic AGOs. a, Cluster of eukaryote-specific insertion segments between the L1 and PIWI domains in the binary KpAGO complex. Arg 227, Arg 732, Asp 1128, Asp 1138, Asp 1168 and Gln 1171 are conserved among eukaryotic AGOs. **b–d**, Comparison of the nucleic-acid-binding channels in the binary KpAGO complex (**b**), the binary TtAGO complex (**c**) and the ternary TtAGO complex (**d**). This view down the nucleic-acid-binding channel shows that there is no obstruction by the KpAGO N domain (cyan), whereas the TtAGO N domain blocks one end of the nucleic-acid-binding channel in both the binary and ternary complexes. Colours are as in Fig. 2a. Guide and target strands are coloured in red and slate, respectively.

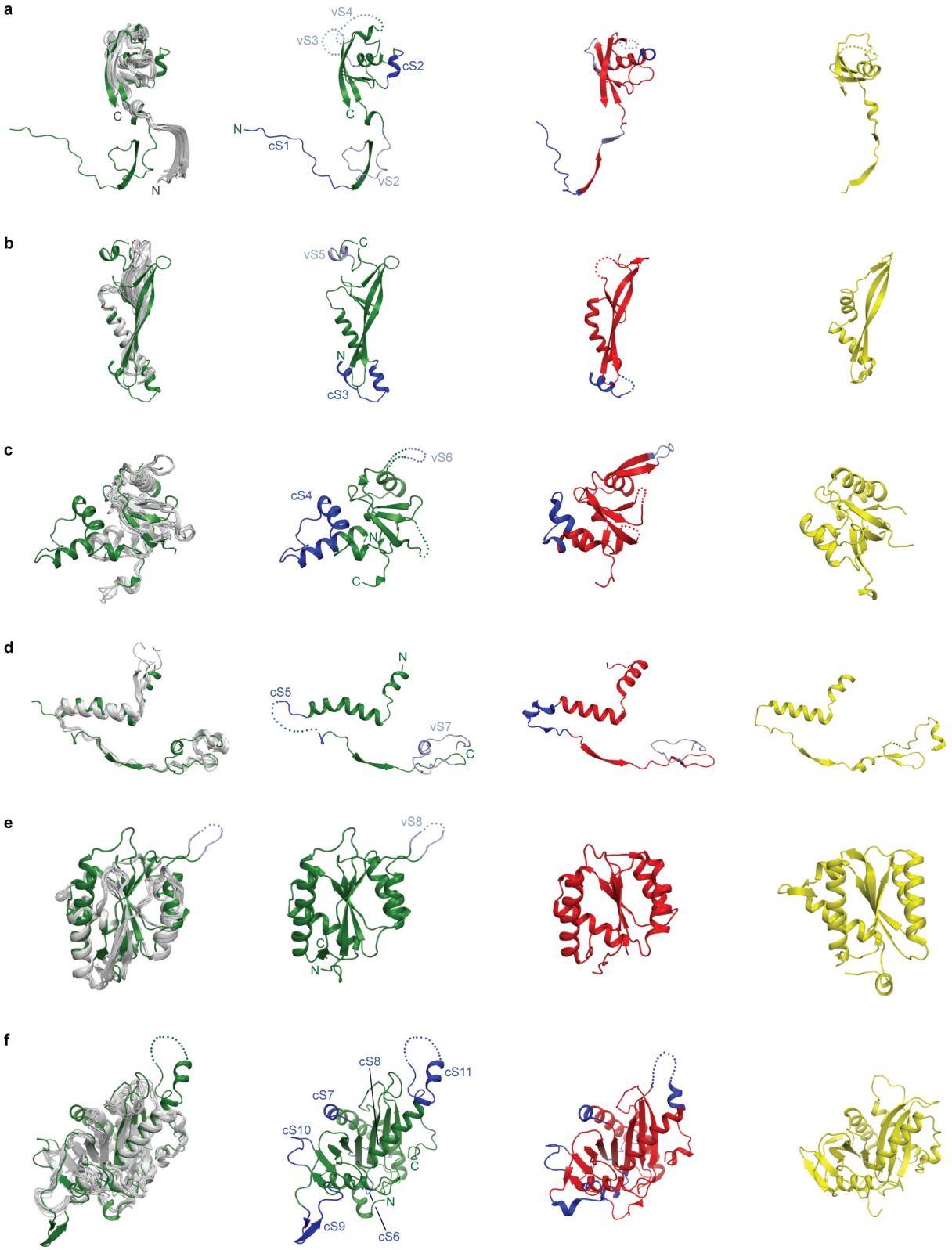
a
vS4
vS3
cS2
C
N
cS1
vS2
C
N
b
vS5
C
N
cS3
c
vS6
cS4
N
C
d
N
cS5
vS7
C
e
vS8
C
N
f
cS8
cS11
cS7
cS10
C
N
cS9
cS6

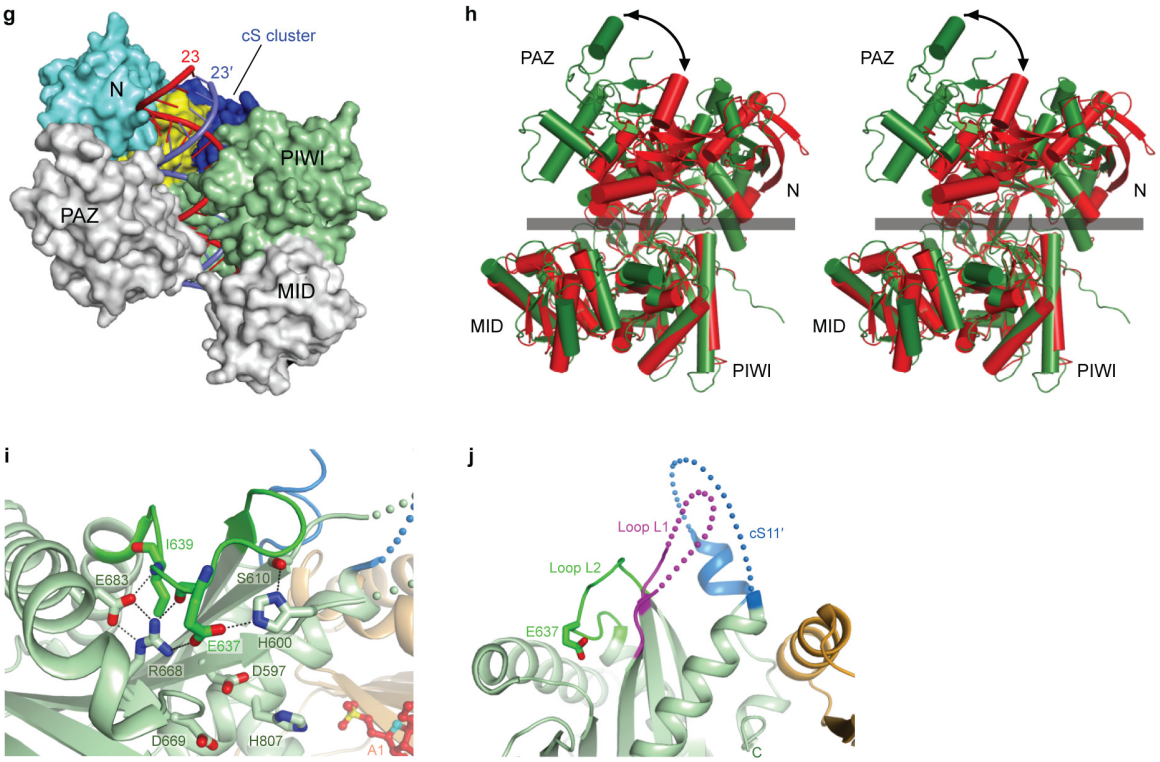

Supplementary Figure 14 | Structural comparisons with HsAGO2. a–f, Superpositions of the TtAGO (gray), KpAGO (green), HsAGO2 (red) and *P. furiosus* AGO (yellow) structures on their N (**a**), L1 (**b**), PAZ (**c**), L2 (**d**), MID (**e**) and PIWI (**f**) domains. Constant (cS) and variable (vS) insertion segments in eukaryotic AGOs are coloured in blue and slate, respectively. Disordered regions are drawn as dotted lines. All 11 of the conserved insertion segments in KpAGO, as well as many of the variable insertion segments, are also found in HsAGO2. **g**, HsAGO2 with modelled A-form duplex, revealing an extended and potentially unobstructed nucleic-acid-binding channel. Protein surfaces are rendered, highlighting the cS cluster that extends the channel (blue). **h**, Superposition of KpAGO (green) and HsAGO2 (red) based on the MID-PIWI lobe. The nucleic-acid-binding channel is highlighted (gray bar). A rotation in the relative orientation of the PAZ domain is indicated (black arrows). **i**, Hydrogen-bond network stabilizing the plugged-in loop L2 with the Glu 637 finger, depicted as in Fig. 5b. **j**, Conformation of the loop L1 gate, depicted as in Fig. 5c. The HsAGO2 segment corresponding to KpAGO cS11 (cS11′) contained four mutations (S824A/S828D/S831D/S834A) with unknown functional consequences.